Article

Motion-unrestricted dynamic electrocardiogram system utilizing imperceptible electronics

Check for updates

Ding Li[1,5], Tian-Rui Cui[1,5], Jia-Hao Liu[2,5], Wan-Cheng Shao[1,5], Xiao Liu[2], Zhi-Kang Chen[1], Zi-Gan Xu[1], Xin Li[1], Shuo-Yan Xu[1], Zi-Yi Xie[2], Jin-Ming Jian[1], Xu Wang[2], Lu-Qi Tao [3], Xiao-Ming Wu[1,3], Zhong-Wei Cheng[4], Zi-Rui Dong[1], Hou-Fang Liu [3] ✉, Yi Yang[1,3] ✉, Jun Zhou [2] ✉ & Tian-Ling Ren [1,3] ✉

Electrocardiogram (ECG) plays a vital role in the prevention, diagnosis, and prognosis of cardiovascular diseases (CVDs). However, the lack of a user-friendly and accurate long-term dynamic electrocardiogram (DCG) device in motion has made it challenging to perform many daily cardiovascular risk screenings and assessments, such as sudden cardiac arrest, resulting in additional economic burdens on society. Here, we present a motion-unrestricted dynamic electrocardiogram (MU-DCG) system, which employs skin-conformal, imperceptible electronics for long-term, comfortable, and accurate 12-lead DCG monitoring. To facilitate assembly for use on the skin, the MU-DCG system features a pressure-activated flexible skin socket for stably soft-connecting the on-skin soft module and the off-skin stiff module during dynamic movements. Crucially, blinded cardiologist evaluations confirm minimal motion artifacts in MU-DCG-acquired ECG signals. Our results demonstrate that the MU-DCG system, with large-area, ultra-thin on-skin electrodes/leads, and an off-skin module, accomplishes anti-motion interference acquisition and in-situ analysis while retaining wearing imperceptibility.

Cardiovascular diseases (CVDs), the leading cause of global mortality[1], develop in diverse ways, ranging from gradual and subtle changes like hypertension to sudden and dramatic events like cardiac arrest[2,3]. Early detection and timely intervention are critical for reducing the CVD mortality rate[4,5]. Electrocardiogram (ECG) reflects the electrical activity of the heart, with abnormalities directly linked to heart diseases. Dynamic electrocardiogram (DCG) monitoring, which involves continuous ECG recording, serves as a widely used non-invasive diagnostic tool for CVDs[2,6–8]. Conventional DCG systems typically contain ten button electrodes attached to the chest and ten enameled leads. However, non-stretchable electrodes and the bulky lead wires restrict the wearer's motion and introduce additional interference, which hinders DCG systems from applying in wider dynamic scenarios[9,10]. Attempts to improve portability by reducing the number of leads (only retain 1–3 leads)[11–13] compromise the diagnostic gold standard of 12-lead ECG, leading to ambiguity and reduced acceptance among cardiologists[14–16]. While advancements have been made in electrode/lead design for 12-lead DCG, existing solutions often rely on adhesives

[1]School of Integrated Circuit, Tsinghua University, Beijing, China. [2]School of Information and Communication Engineering, University of Electronic Science and Technology of China, Chengdu, China. [3]Beijing National Research Center for Information Science and Technology (BNRist), Tsinghua University, Beijing, China. [4]Department of Cardiology, Peking Union Medical College Hospital, Chinese Academy of Medical Sciences and Peking Union Medical College, Beijing, China. [5]These authors contributed equally: Ding Li, Tian-Rui Cui, Jia-Hao Liu, Wan-Cheng Shao. ✉e-mail: houfangliu@tsinghua.edu.cn; yiyang@tsinghua.edu.cn; zhouj@uestc.edu.cn; rentl@tsinghua.edu.cn

for bulky components[17], tight-fitting garments[18,19], or non-standard electrode placement[20], all of which limit wearability and hinder reliable long-term monitoring during movement[21].

As a burgeoning technology, epidermal electronics offer a promising solution for wearable health monitoring. However, while existing researches have primarily focused on device optimization, there remains a dearth of comprehensive system-level solutions. Epidermal electronics boast skin conformability and the ability to capture various physiological signals, including metabolic biomarkers[22,23], bioelectricity[24,25], and biological movement[26,27]. These ultrathin, lightweight, soft, and skin-like designs enable imperceptible wearability and accurate signal acquisition[26,28-31]. Nevertheless, integrating flexible and stiff components on a single flexible substrate (with a patch-like appearance) is difficult in reconciling conformability with stability[25,32-34]. To address this, a "soft-stiff separation" structure has emerged, positioning conformal epidermal sensors directly on the skin and other components off the skin[35-38]. While enhancing imperceptible wearability, the structure necessitates robust interconnection between on-skin and off-skin components for assembly use. Conventional connecting methods like welding, hot-pressing bonding, or mechanical locking often compromise skin integrity and the conformability of imperceptible electronics during assembly. Consequently, developing a robust system that employs imperceptible electronics while withstanding motion and skin irregularities remains a significant challenge[37-39].

Here, we present the first-ever motion-unrestricted dynamic electrocardiogram (MU-DCG) system, enabling imperceptible 12-lead DCG monitoring during daily activities. This system embodies an imperceptible human-machine fusion concept, seamlessly integrating imperceptible wearability, dynamic monitoring, and in-situ disease analysis to function as an "invisible doctor" for continuous health monitoring (Fig. 1a). The MU-DCG system comprises on-skin conformal components, a flexible skin socket, and an off-skin module (Fig. S1). By leveraging polymer fiber films—a controllable, ultrasoft, and inexpensive substrate for on-skin components[26,40,41]—combined with helical interconnects[42], we achieve an imperceptible wearable experience and high-quality 12-lead DCG acquisition even during motion. Additionally, the MU-DCG system incorporates a flexible skin socket with a simple three-layer, pressure-activated design, allowing users to effortlessly and freely assemble on-skin components and connect them to off-skin processing circuits. The off-skin module enables in-situ disease analysis, facilitating real-time response, low-power consumption, and user privacy protection. The MU-DCG system achieves an combination of an ultra-thin profile (< 50 μm), large-area skin coverage, flexibility, and breathability, while also being the first to integrate in-situ disease analysis (Table S1). This unique integration offers significant potential for exploring motion-induced cardiac conditions and revolutionizing cardiac monitoring in demanding scenarios where motion-unrestricted cardiac monitoring is paramount, such as athlete assessment, aerospace missions, and emergency rescue.

Results

Concept and realizing strategy of the MU-DCG system

Figure 1b illustrates a subject wearing the MU-DCG system comfortably. Compared to existing 12-lead ECG collection devices, the MU-DCG system eliminates cumbersome electrodes and lead wires by utilizing imperceptible electronics (Fig. S2). In the MU-DCG system, the V1–V6 electrodes are positioned slightly lower on the chest than in the standard Holter configuration (Fig. S3). This deliberate design choice facilitates the routing of the flexible on-skin interconnects along the chest midline, enabling seamless integration and minimizing discomfort during movement[43]. While minor amplitude variations are observed in the V1–V3 leads, the morphological comparison of 12-lead ECG signals demonstrates excellent agreement between the MU-DCG and Holter systems, particularly for the clinically crucial inter-peak segments, including the PR and ST segments and the PR interval (Fig. S4). This preservation of key morphological features, which are essential for clinical diagnosis across multiple leads, confirms the clinical relevance of the MU-DCG system[44,45]. Stiff computing
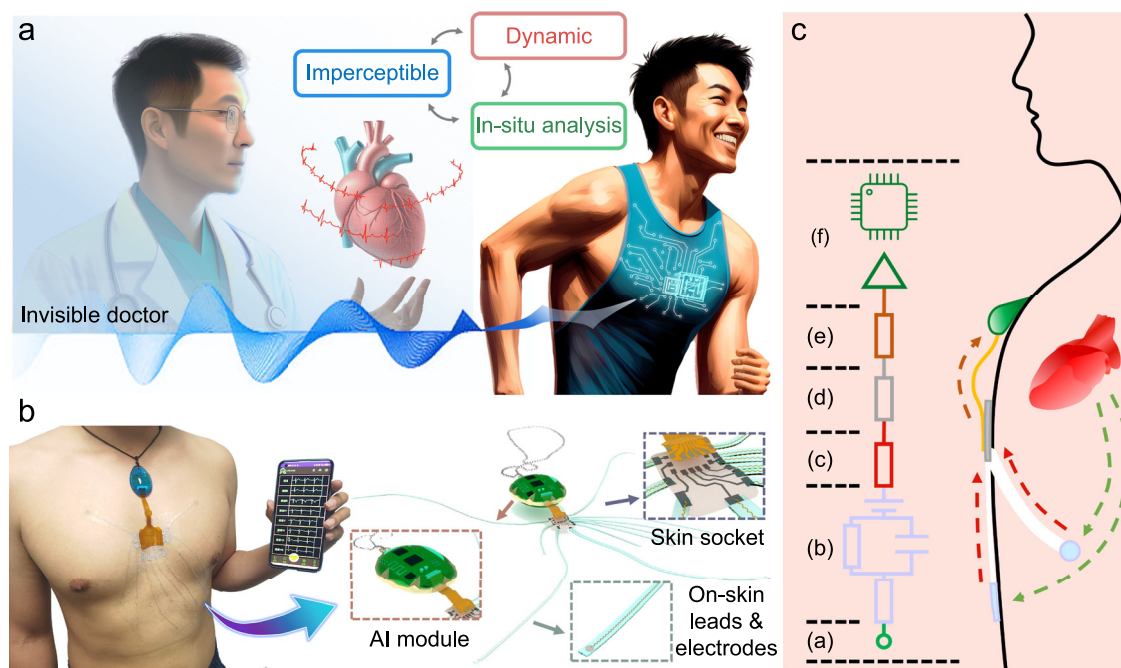

Fig. 1 | Conceptual illustrations and images of the MU-DCG system. a The imperceptible human-machine fusion system accomplishes real-time acquisition and in-situ analysis of physiological data while retaining imperceptibility like an invisible private doctor. **b** A subject wearing an MU-DCG system (left). The enlarged view of the device structure (right). **c** Circuit model of the signal acquisition and process in the MU-DCG system: **a** the signal source, **b** the electrode-skin interface, **c** the lead wire/interconnect, **d** the flexible skin socket, **e** the FPCB plug, **f** the in-situ analysis module in the pendant.

components and the battery are integrated into the blue pendant off the skin, reducing the skin burden. A flexible printed circuit board (FPCB) plug is attached to the skin to receive multi-channel ECG signals. The user-friendly assembly process (Movie S1) involves first attaching the flexible skin socket to the chest, followed by connecting the on-skin electrodes and leads. The video demonstrates a 10-electrode configuration for 12-lead ECG, which can be readily adapted to different electrode counts as needed. Finally, the FPCB plug of the off-skin module is connected to the flexible skin socket. Therefore, the MU-DCG system surpasses existing devices by offering imperceptible and motion-unrestricted wearability, and achieving state-of-the-art performance in dynamic monitoring and in-situ disease analysis (Fig. S2).

The on-skin electrodes and leads come as a single, disposable, all-in-one component integrating silver nanowire (AgNW) electrodes, helical copper (Cu) fiber interconnects, and liquid metal (LM) plugs on the fiber film substrate (Fig. S5). The AgNW electrodes, formed by drop-coating an aqueous AgNW solution, avoid the use of substrate-damaging organic solvents and high-temperature processes. Based on low-cost, mature industrial products, the helical Cu fiber interconnects exhibit reliable performance and convenient fabrication (Fig. S6). The preparation and use of the temporary transfer substrate address the challenge of transferring ultrathin on-skin components onto the skin (Fig. S7). These designs ensure flexibility, self-adhesion, and breathability for imperceptible and motion-unrestricted wear (Figs. S8–10, Movie S1).

The MU-DCG system bridges on-skin and off-skin components using a flexible skin socket. This self-adhesive, skin-conformable film forms a secure and stable connection with the LM plug of the on-skin component. It also transmits multichannel ECG signals to the off-skin module through the FPCB plug. The off-skin module, equipped with a self-developed biomedical processor, provides complete signal acquisition and in-situ disease analysis[46,47].

A equivalent circuit model of the signal transmission path in the MU-DCG system is shown in Fig. 1c. Maintaining signal chain stability is paramount for high-fidelity ECG acquisition. Biological potential signals originating from the heart (a) first traverse the electrode-skin interface. This interface introduces potential from the electrical double layer, capacitance/resistance related to the contact, and electrode resistance (b). The signal then sequentially passes through the lead wire and LM plug (c), the flexible skin socket (d), and the FPCB plug (e) before reaching the off-skin processing unit (f). Among these, four key components (b–e) in the MU-DCG system have been optimized to enhance signal stability: the integrated electrode-lead design (b), previously detailed in our prior work[42]; the lead wire/LM plug (c) and flexible skin socket (d) described in the following sections; and industrially robust FPCB plug (e), ensuring reliable conductivity.

Design and performance of the flexible skin socket

The flexible skin socket comprises three layers: a polyurethane (PU) fiber film substrate, a gallium indium eutectic (LM) conductive layer, and a PDMS adhesive layer (fabrication details provided in Methods). The LM layer, fabricated by ultrasonically treating gallium indium eutectic in ethanol and subsequent spraying onto the PU film, forms micro-conductive channels when plugs are attached under pressure. This mechanism relies on the inherent flowability of the LM combined with the non-uniform thickness of the PDMS adhesive layer, as illustrated by finite element simulations (Fig. S11). In practical device fabrication, Fig. 2a shows the structure of three activated sockets with varying adhesive layer thicknesses and corresponding energy-dispersive spectroscopy (EDS) element distribution maps. The socket with the thinnest adhesive layer exhibits insufficient adhesion due to complete Ga element coverage, while the one with the thickest adhesive layer forms limited micro-conductive channels, compromising conductivity. The optimal socket design features a moderate

adhesive layer thickness, balancing adhesion and conductivity by maintaining approximately 50% adhesive area and numerous micro-conductive channels. Figure 2b demonstrates the relationship between adhesive layer thickness and connection conductivity. Increasing the PDMS/hexane concentration initially elevates resistance, followed by a loss of pressure-activated conduction and eventual insulation. The optimal concentration (around 15%) ensures a continuous adhesive layer while permitting the formation of micro-conductive channels under pressure (Fig. 2c).

The skin socket serves as an interface between the on-skin soft module and the off-skin stiff module, i.e., flexible and stiff components in the MU-DCG system are integrated through the skin socket. LM plugs of the on-skin flexible components form a soft-soft connection with the skin socket, and FPCB plugs of the off-skin stiff module form a soft-stiff connection with the skin socket (Fig. S12). To assess the performance of the soft-soft connection, the LM plugs were attached to the flexible skin socket via finger pressure and subjected to stretchability tests. As a control, common conductive tapes underwent the same test. Figure 2d presents that the average electrical and mechanical stretchability of the flexible skin socket connection reaches 246% and 247%, respectively, surpassing the control group by five times (carbon tape: electrical stretchability ~ 20%, mechanical stretchability ~ 40%). Figure 2e illustrates the absolute change in resistance of these connections under ultimate strain. The flexible skin socket connection maintained a resistance change below 20 Ω even when stretched to 85 mm (30 mm origin length), while other connections exhibited significant resistance increases or failures during the initial stretching. As shown in the right magnified graph, Cu tape, conductive fabric tape, and anisotropic conductive film (ACF) lose their conduction in the first 2 mm stretching process. For the carbon tape, its resistance first drops by about 1 MΩ, followed by rapid insulation at 8 mm. Repeated bonding and tensile tests demonstrated the durability of the soft-soft connection with minimal resistance variation (Fig. 2f). Figure 2g presents the result of 1000 cycles of the 50% strain tensile test. The magnified insets demonstrate that the conduction resistance fluctuates within 0.5 Ω with a baseline drift of about 0.4 Ω.

Building upon the flexible skin socket, a soft-stiff connection has been implemented to transmit multi-channel ECG signals collected by the on-skin electrodes to the off-skin module. As illustrated in Fig. 3a, a patterned flexible skin socket forms a soft-stiff connection with the FPCB plug, which serves as a buffer between the on-skin components and the off-skin module. Ten copper electrodes distributed at the end of the FPCB plug contact directly with the skin socket to receive the multi-channel ECG signal. In the center of the FPCB plug, an indicator LED is designed to remind the user when the skin socket is activated. The other end of the FPCB plug is connected to the pendant. The patterned flexible skin socket interfaces with the LM plug of the on-skin electrodes/leads through larger external electrodes, while smaller internal electrodes are designed to connect the FPCB plug. The skin socket exhibits excellent flexibility, withstanding 50% strain and 90-degree torsion. Its ultra-thin profile (< 50 μm) and low Young's modulus (approximately 145 kPa) ensure conformal contact with the skin and minimize discomfort (Fig. S13).

To evaluate the adhesion of the soft-stiff connection between the skin socket and the FPCB plug, various tests were performed. Figure 3b presents the force-stroke curves with and without skin attachment. The blue and orange curves illustrate the results of the flexible skin socket attachment/non-attachment to the skin, respectively. The skin-attached connection demonstrates a higher peak peel force and occurred earlier in the test, indicating stronger adhesion. Calculating the area under the curve revealed greater adhesion energy for the skin-attached connection, likely due to improved contact under pressure. Repeated peel tests demonstrate the consistent adhesion of the connection (Fig. 3c). To simulate daily use, a customized motion acquisition system was used to measure the swing range of the pendants
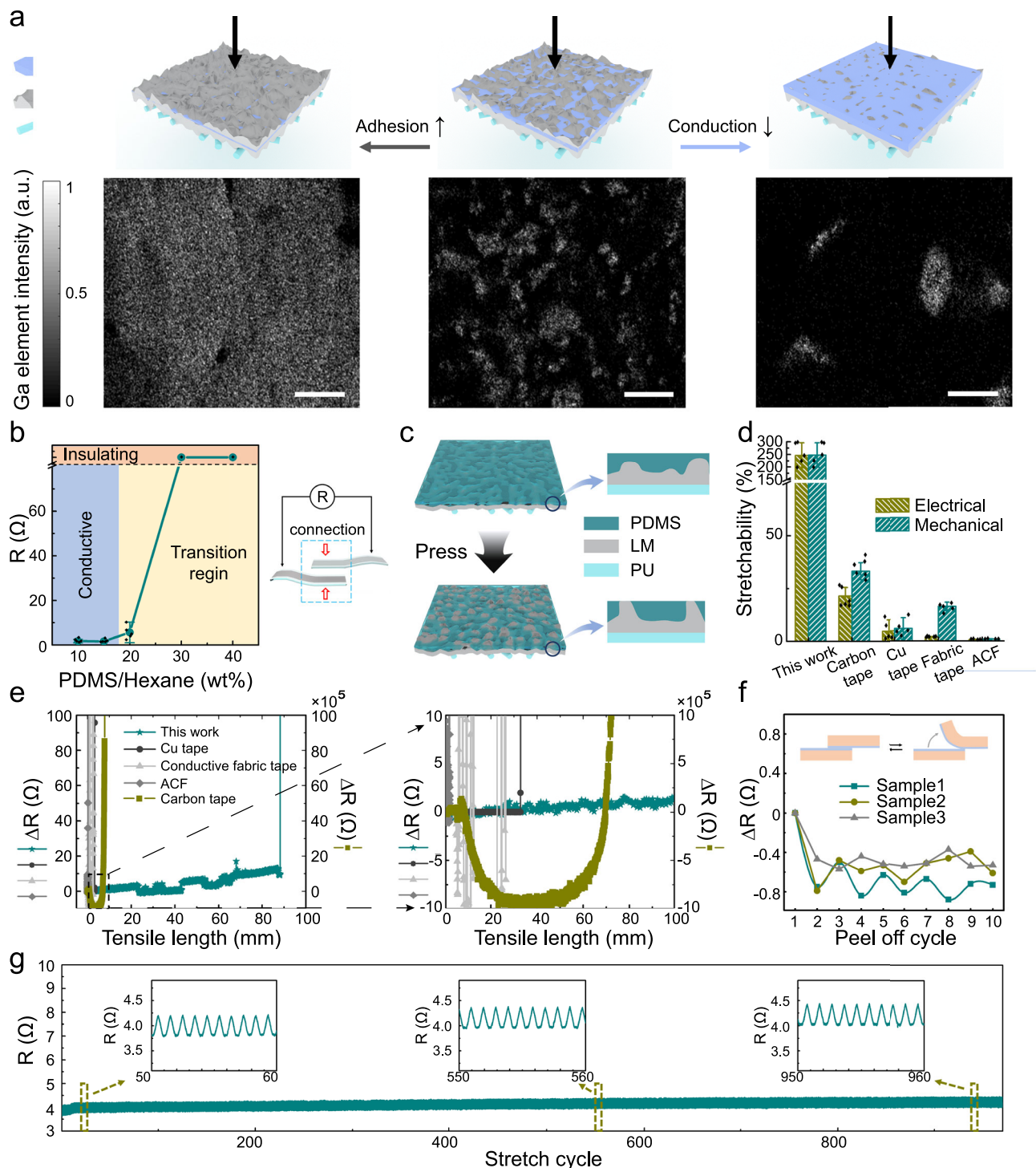
Fig. 2 | Structural of the flexible skin socket and performances for the connection between skin sockets and the on-skin component's LM plugs (soft-soft connection). a The flexible skin socket has a three-layer structure. The PDMS layer's thickness affects the socket's adhesion and conduction. EDS surface element analysis illustrates the microscopic conduction mechanism of the flexible skin socket. Similar results were obtained from 10 independent replicate experiments. Scale bar, 20 μm. **b** Relationship curve between conduction resistance of the connection and PDMS dip coating concentration. Error bars are s.d. from 5 device samples and the central line represents the mean value. The inset on the right illustrates the measurement setup (overlapping area 2 cm width × 3 cm length). **c** The pressure-activated conduction mechanism of flexible skin sockets: LM micro-conductive channels are established by pressure. **d** The electrical and mechanical stretchability of the flexible skin socket and commercial tapes. The flexible skin socket connection showed greater average electrical (246%) and mechanical (247%) stretchability (overlapping area 2 cm width × 3 cm length). Error bars are s.d. from device samples $n = 5$ for this work, fabric, and Cu tape, $n = 6$ for Carbon tape, $n = 4$ for ACF. **e** The absolute change in resistance of different connections during the ultimate strain test. Unlike commercial tapes, the flexible skin socket connection remained stably conductive (resistance change within 15 Ω) even at 80 mm tensile length as shown in the image on the left (the origin length of all samples is 30 mm). The magnified image of the low tensile length region (0–10 mm) on the right shows the flexible skin socket connection experienced < 2 Ω change in resistance at 10 mm tensile length. **f** Cyclic bonding tests for the flexible skin socket connection. Three samples show stable conduction resistance during bonding and peeling cycles. **g** The 1000 cycles of 50% strain tensile test for the flexible skin socket connection. The fluctuation of the conduction resistance is within 0.5 Ω, and the baseline drift is about 0.4 Ω.
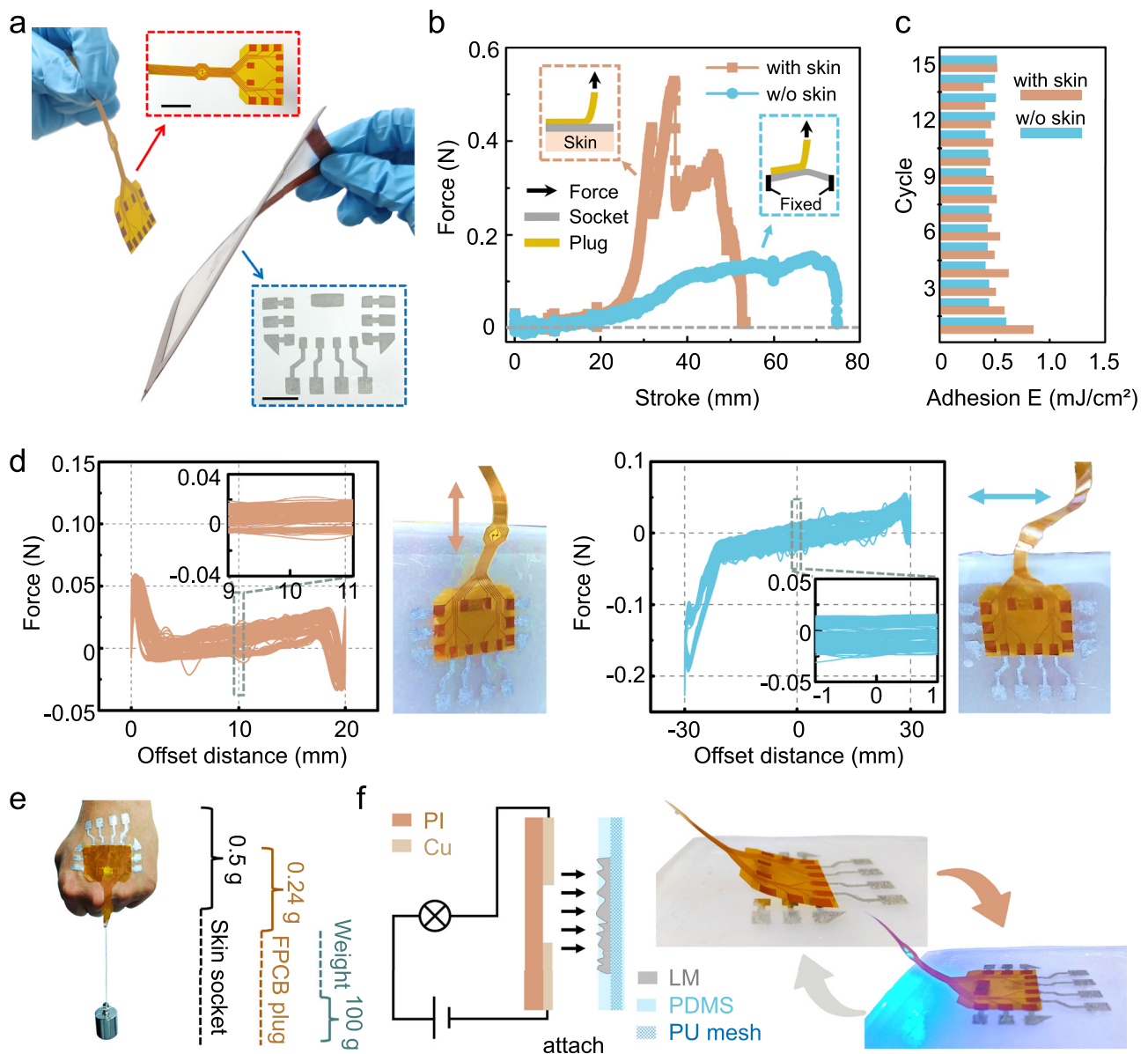
Fig. 3 | Illustrations and performances of the connection between skin sockets and FPCB plugs (soft-stiff connections). a An image of a soft-stiff connection formed by a patterned skin socket (right) and an FPCB plug (left). The upper inset is the enlarged view of an FPCB plug. The bottom inset is the enlarged view of a patterned skin socket. Scale bar, 2 cm. **b** Stroke-force curves, peeling the FPCB plug from the skin socket. **c** Cyclic adhesion energy test (carried out on and off the skin) for the soft-stiff connection. **d** The 1000 cycles of lateral and longitudinal drag test. **e** An image shows that a soft-stiff connection withstands the tangential stress caused by a 0.1 kg weight. **f** Circuit diagram of the conducting indicator light in the soft-stiff connection and the images of the indicator LED when attaching and peeling.

(Fig. S14). Figure 3d shows the force recordings for 1000 cycles of lateral and longitudinal drag tests according to the swing range. The connection remained stable after the fatigue testing, and no detachment was observed during this process. Figure 3e presents a weight-bearing test of a soft-stiff connection, demonstrating the connection's robustness, with a 0.1 kg weight suspended from the FPCB plug. Figure 3f depicts the circuit diagram of the conducting indicator LED, which illuminates upon the successful connection of the FPCB plug to the skin socket. In addition, we conducted comprehensive pressure tolerance testing on the skin socket. The internal wiring of the skin socket, the connection between the skin socket and the FPBC plug (soft-stiff connections), and the connection between the skin socket and the on-skin all-in-one component's plug (soft-soft connections) were evaluated (Fig. S15). Multiple samples maintained stable conductivity at 400 kPa during the incremental pressure testing. After 1000 cycles of 400 kPa pressure testing, the conductivity of the

internal wiring and the connections with the plugs remained stable (Fig. S16), demonstrating robust performance under repeated pressure.

Dynamic Acquisition and Real-time In-Situ Analysis

A proposed myocardial infarction (MI) detection algorithm based on 12-lead ECG is presented in Fig. 4a. The 12-lead ECG data collected by the MU-DCG system reflects the status of the heart from multiple perspectives. The 12-lead ECG pre-processed data are fed into a lightweight MI classification convolutional neural network (CNN), which consists of three lightweight convolutional blocks and two fully connected layers. Feature maps of the last convolutional layer pass through a fully connected neural network and a Softmax layer to output the predicted results. Compared to traditional CNNs, this streamlined CNN architecture significantly reduces the number of parameters and computational complexity (Supplementary Methods
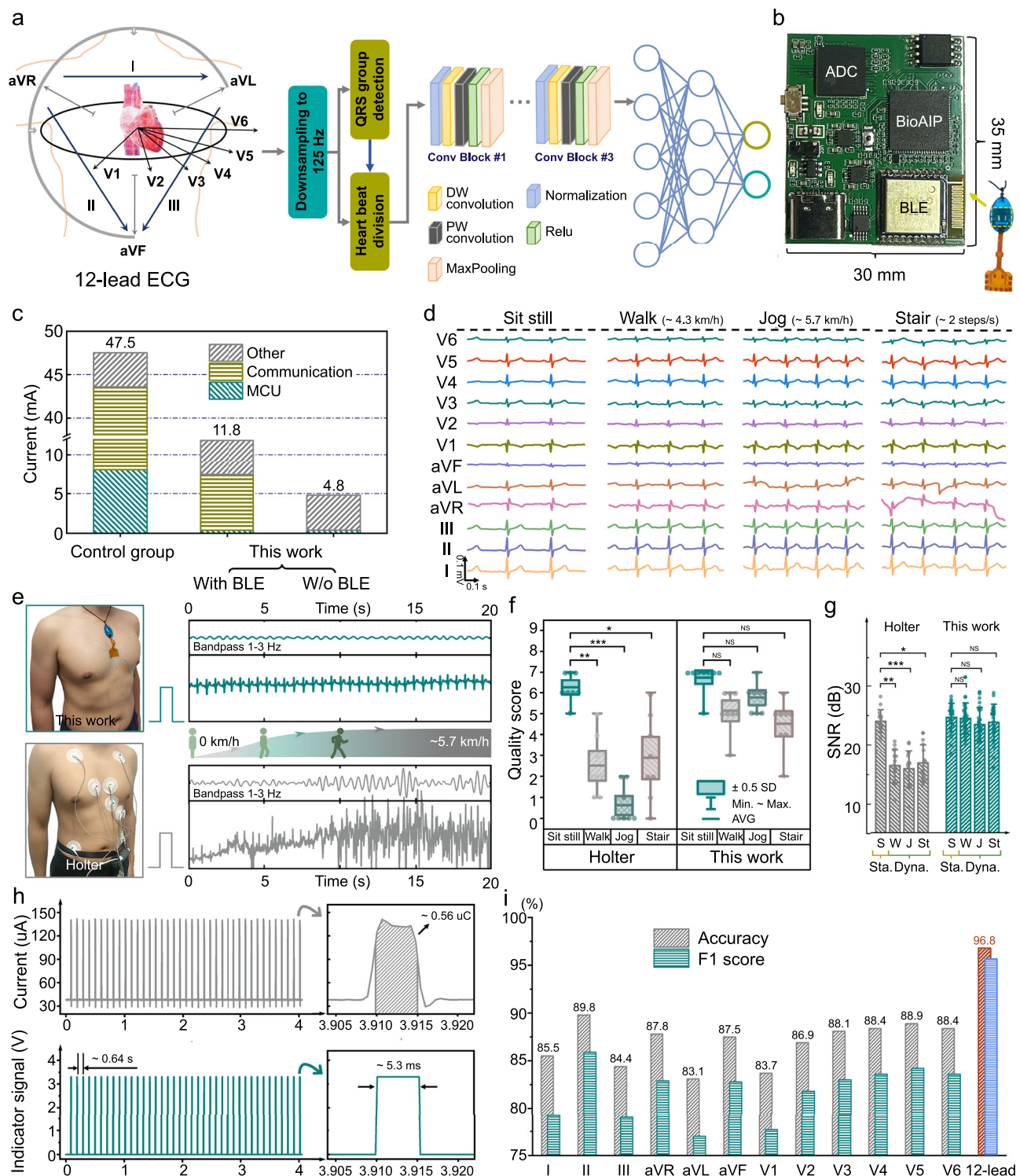
and Table S2). Therefore, this algorithm can be fully deployed in the off-skin module to realize edge computing.

The off-skin module enables real-time and low-power ECG analysis. As shown in Fig. 4b, the size of the module is 30 mm × 35 mm, which integrates a self-developed biomedical artificial intelligence processing (BioAIP) SoC (system-on-chip), an analog-to-digital converter (ADC), a Bluetooth, a flash and power management circuits (Fig. S17). Due to the in-situ processing of the 12-lead ECG data, the MU-DCG system can adopt Bluetooth Low Energy (BLE) only to transmit the in-situ processing results. A comparison group using a conventional microcontroller unit (MCU) and Bluetooth 2.0 serves as

a benchmark (Fig. S18). As shown in Fig. 4c, even when deployed with MI classification algorithms, the MCU (BioAIP) power consumption of the MU-DCG system remains lower than that of the control group. Independent operation and BLE sleep mode further extend battery life, achieving a 10-fold increase in endurance compared to the control system (4.8 mA operating current). The proposed MU-DCG system exhibits the lowest per-channel power consumption compared to two commercial Holter devices and a flexible 12-lead ECG system from our previous work (Table S3). By eliminating the need for cloud-based data transmission, in-situ analysis performed directly by the off-skin module greatly shortens the response time,

Fig. 4 | Illustrations of the off-skin module and performances of the MU-DCG system. a The lightweight CNN that supports in-situ analysis of 12-lead ECG signals. **b** Images of the main components of the AI module (left) and the off-skin pendant (right). **c** The working current comparison between the MU-DCG system (the experimental group) and the control group. The current was measured under a 3.7 V power supply. **d** 12-lead ECG waveforms captured by the MU-DCG system during sitting still, walking, jogging, and up/down stairs. **e** Lead-II ECG signals were measured by the Holter and the MU-DCG system during the process from stationary to jogging. The signals are bandpass filtered at 1–3 Hz to extract the low-frequency components. Scale amplitude 2 mV. **f** Statistical chart of ECG waveform quality score for the Holter and the MU-DCG system by cardiologists under different conditions (blind evaluation experiment). Data samples $n = 8$ were randomly selected from the data tested on three subjects for every box plot; Each box plot represents the mean (central line), half of the standard deviation (box edges), and max/min (whiskers). Statistical significance was assessed using the Kruskal-Wallis Test; $*p = 0.04206$, $**p = 0.0108$, $***p = 8.73349 \times 10^{-5}$; NS: no significant difference. **g** The SNR of the MU-DCG system is compared with that of Holter under static and dynamic conditions. S: sit still, W: walk, J: jog, St: Stair. Sta. and Dyn. are abbreviations of static and dynamic respectively. Data samples $n = 15$ for Holter and $n = 35$ for this work, which were randomly selected from the data tested on three subjects. Bar height, mean; error bars are s.d.; Statistical significance was assessed using the Kruskal-Wallis Test; $*p = 0.00127$, $**p = 5.29036 \times 10^{-5}$, $***p = 2.89351 \times 10^{-5}$; NS: no significant difference. **h** The classification time and working current test results of the 12-lead ECG data by the BioAIP chip. **i** Comparison of the recognition accuracy and F1 score of the MI using single-lead and 12-lead ECG data respectively.

reduces transmission power consumption, and effectively safeguards user privacy (Fig. S19).

The MU-DCG system captured 12-lead ECG signals when subjects were sitting, walking, jogging, and ascending/descending stairs, respectively (Fig. S20–21 and Movie S2). Part of the data (from user#1) is shown in Fig. 4d. Increasing exercise intensity correlated with higher heart rate, but clear ECG waveforms were maintained across all activities. A comparative study with a medical Holter monitor was conducted (Fig. S22–25). Figure 4e demonstrates the impact of motion on ECG signal quality. The Holter suffered from motion artifacts, particularly during exercise, while the MU-DCG maintained signal integrity. The signal components obtained through bandpass filtering at 1–3 Hz demonstrate that the ECG signals collected by the MU-DCG system have less low-frequency baseline drift interference. Cardiologist assessments confirmed by cardiologists in Fig. 4f present that the quality of the ECG signal collected by the MU-DCG system is consistent with that of the Holter in the resting state (Table S4 for the score criteria form). However, Holter suffers significant signal interference under dynamic states due to the electrode-skin mismatch and lead wires' dragging/tangling. A comparison with an ECG pectoral girdle device (using dry electrodes) further confirms the superior integrity of dynamic ECG signals captured by the MU-DCG (Fig. S26–28). The signal-noise ratio (SNR) analysis results in Fig. 4g prove that MU-DCG systems provide better dynamic noise resistance performance. Compared with the static condition (average SNR ≈ 25 dB), the SNR of the dynamic ECG signal collected by the Holter has obvious attenuation (average SNR < 17 dB) while the MU-DCG system still acquires high-quality ECG signals (average SNR > 23 dB). The ECG pectoral girdle system exhibited lower SNRs in both static (average SNR < 17 dB) and dynamic (average SNR < 13 dB) conditions (Fig. S29).

User comfort was evaluated by comparing the MU-DCG system with three existing wearable ECG devices: Holter monitors, single-lead ECG patches, and ECG pectoral girdles (Fig. S2). 12 volunteers participated in one-hour wear trials with each device. Discomfort levels were assessed using the validated visual analog scale (VAS)[36], with participants rating their experience on a scale from 0 (no discomfort) to 10 (maximum discomfort). Data from 11 participants were deemed valid for analysis. The MU-DCG system achieved the lowest mean VAS score of 0.55, indicating superior user comfort compared to the other devices (Fig. S30).

The off-skin module's capability for real-time, low-power 12-lead ECG data analysis was evaluated. Figure 4h presents the performance metrics of the BioAIP executing the MI detection algorithm (additional classification results for heartbeats are provided in Fig. S31 and Table S5). The chip operated at an average current of 37.6 µA, consuming 0.56 µJ per classification at 1 V supply voltage, with a classification time of 5.3 ms (detailed performance in Figs. S32–34). In addition, the necessity of 12-lead ECG acquisition and analysis was demonstrated through comparative experiments. Myocardial-ischemia-caused myocardial infarction (MI) can manifest in various cardiac regions (anterior, posterior, lateral, or combined), thus specific ECG features may only appear in certain leads. As shown in Fig. 4i, the MU-DCG system with standard 12-lead ensures higher MI detection accuracy (96.8%) compared to single-lead ECG devices (maximum accuracy of 89.8% by lead II).

Discussion

We have demonstrated that the MU-DCG system represents a paradigm shift in long-term, 12-lead ECG monitoring by seamlessly integrating imperceptible on-skin conformal electronics, pressure-activated skin sockets, and in-situ disease analysis. This "invisible doctor" system offers superior comfort, accuracy, safety, and long-term wearability, enabling continuous, motion-unrestricted ECG monitoring in daily activities for enhanced medical diagnosis and research. The MU-DCG system not only holds immense promise for enhanced medical diagnosis and research but also establishes a groundbreaking design strategy for future human-machine fusion healthcare applications. The system's capacity of integrating imperceptible electronics, user-friendly assembly, and in-situ processing opens exciting avenues for the development of continuous, personalized health monitoring solutions across diverse settings. In future iterations, advanced manufacturing techniques, such as LM selective wetting for interconnects formation[48,49], and three-dimensional printing technology[50] will be explored to further optimize system performance and expand its potential applications.

Methods
Material preparation
The polydimethylsiloxane (PDMS) precursor is a mixture of the Dow Corning Sylgard 184 silicone elastomer base and curing agent (wt/wt = 10:1). The polyurethane (PU) solution was prepared by mixing PU particles (Tecoflex, code SG-85A) and N, N-dimethylformamide (DMF, from Aladdin) at a weight ratio of 3:17 before magnetic stirring for 3–5 h at 80 °C. The PDMS solution was prepared by diluting PDMS precursor with hexane (Meryer, spectral purity ≥ 97%) in a mass ratio of 1:9, 3:17, and 1:4 (corresponding to 10 wt%, 15 wt%, 20 wt%). The silicone substrate for simulating skin was made of Ecoflex 00-30 (Smooth-on Inc., USA) in a 1:1 mass ratio. The water-based silver nanowire (AgNW) solution (diameter 100–150 nm, 10 mg/mL) was purchased from XFNANO (Nanjing, China) Materials Technology Corporation. The gel electrode used in this article was purchased from Hangzhou Xunda Radio Equipment Co., Ltd. China, and it meets the medical devices standards of the National Medical Products Administration of China. The copper fiber (diameter 50 µm) that makes up the on-skin helical interconnects was purchased from Guantai (Xingtai, China) Metal Materials Corporation. The liquid metal (LM, Ga 75.5% / In 24.5%, ≥ 99.99% purity) was purchased from Sigma-Aldrich. The medical-grade conductive hydrogel used for AgNW electrode pretreatment was obtained from Suzhou Letai Medical Technology Co., Ltd., which meets the medical device standards of the National Medical Products Administration of China. The sprayed LM solution was made of LM and ethanol in a ratio of 3.6 g to 1 mL, 2 mL, and 3 mL. The

mixture of LM and alcohol needs to be ultrasonically treated for 1 h to disperse the LM, while ultrasonic again for 10 min before each use to prevent precipitation (120 W 40 kHz ultrasonic cleaning machine).

Fabrication of the PU fiber mesh

The PU fiber film was prepared by the electrospinning machine (Beijing Yongkang Leye Technology Development Co., Ltd, China). The specific preparation parameters are as follows: the surface of the drum receiver (10 cm diameter and 20 cm height) was covered with aluminum foil, the speed was 20 r/min, the injection speed of the PU solution (5 mL KDL syringe) was 0.2 mm/min, the needle translation distance was 20 cm, the translation speed was 20 cm/min, the distance between the needle and the drum surface was 16 cm, and the voltage was 10 kV, the needle size was 21 G and the needle length was 13 mm. PU fiber films of different thicknesses were obtained by adjusting the preparation time according to the need.

Fabrication of the flexible skin socket and LM plug used for the test in Fig. 2

Spraying was used to fabricate flexible skin sockets with simple patterns. Using laser etching system (HR-ULS230DT SYS, Universal Laser Systems, USA) to process PDMS hard mask (5 mm thick). The mask plate was placed on the PU fiber mesh where the socket needed to be formed. Note that PU fiber mesh should be placed on dust-free paper to limit alcohol diffusion and make the sprayed pattern more precise. Then the sprayed LM solution was put in a press spray can (50 mL) and sprayed (The use of LM ethanol solutions with different concentrations will ultimately result in LM layers with different surface morphologies, and the details can be found in Fig. S35). Removed the PU fiber mesh sprayed with LM from the dust-free paper and let it stand at room temperature for 10 min until the alcohol evaporates. A film of Teflon (50 μm thick) was placed on the LM coating surface as a temporary protective layer, and a medicine spoon was used to scrape the surface of the Teflon film to activate the LM coating under the Teflon film (the illustrations can be found in Fig. S36). When the temporary Teflon film was removed, a handheld multimeter was used to measure the resistance (< 10 Ω) of the LM coating to ensure that it was activated (the block resistance of the LM layer was measured at this time). Finally, the PU fiber mesh with the activated LM coating was dipped into 15 wt% PDMS/hexane solution 3 times for ~ 3 s each time and then dried in the 70 °C oven for 15 min to remove the solvent and cure the PDMS layer. LM plugs used in the test shared the same fabrication process as the flexible skin socket. In the test of soft-soft connection, the LM plugs and the flexible skin sockets were the same thin-film devices, as shown in the inset of Fig. 2e.

Microscopic characterization of the flexible skin socket

Scanning electron microscope (SEM) and EDS surface element analysis were performed using Zeiss Merlin (Zeiss, Germany). According to the above flexible skin sockets preparation method, three samples with different thicknesses of PDMS layer were prepared (PDMS/hexane solution of 10 wt%, 15 wt%, and 20 wt% were used for the dipping coating process respectively). The three samples were successively placed into the Zeiss Merlin for SEM and EDS observation records. Then the three samples were pressed through the Teflon film with the fingers, and they were returned to the Zeiss Merlin for filming (Fig. S37).

Fabrication of the patterned flexible skin socket used in the MU-DCG system

Screen printing technology was used to transfer designed patterns from mask plates to PU fiber substrates. LM conductive ink was purchased from Beijing Ruozhi Technology Co., Ltd., China. Firstly, the PU fiber mesh ~ 20 μm thick was obtained from the aluminum foil by the PI frame (8 cm × 10 cm × 0.125 mm). After scraping and coating (the mask plate adopts a 200-mesh screen), the PU fiber mesh with patterned LM

coating was put into a 70 °C oven (blast air) for 15 min to remove the solvent. The activation of the LM coating and the production of the adhesive layer were consistent with the fabrication of the flexible skin socket above.

Measurement methods for mechanical properties

The thickness of the PU/PDMS film was measured by a step meter (P17, KLA Tencor, USA). Because PU fiber mesh is a porous and loose structure, it is difficult to use the probe of the step meter to measure, thus the micrometer thickness gauge was used. The PU fiber mesh to be tested was randomly selected 5 points for measurement, and the average value was taken as the reference thickness in this paper. DM3068 Digital Multimeter (Rigol Technologies, China) was used to measure the conduction resistance. The block resistance of the LM layer was obtained by a probe thin layer resistance tester (280SJ, Four Dimensions Inc.). For mechanical characterization of the soft-soft connection and soft-stiff connection, the strain was loaded by AGS-X (Shimadzu, Japan).

Adhesion performance test

Due to the difference in surface morphology, the adhesion performance between the flexible skin socket and the FPCB plug on the skin is different from that of direct testing of the flexible skin socket and FPCB plug adhesion. Therefore, separate tests were conducted. For the "with skin" test, the prepared flexible skin socket was attached to the back of the hand, and then the FPCB plug was attached to the socket. After a certain press to activate the skin socket, the FPCB plug was peeled from the socket by the AGS-X system. During this process, the stroke and adhesion force were recorded. For the "w/o skin" test, the prepared skin socket was suspended and fixed between the two cartons, and the FPCB plug was also attached to the socket. After the socket was activated by applying pressure to the upper and lower surfaces of the connection at the same time with fingers, the FPCB plug was peeled from the skin socket with the AGS-X system, and the stroke and adhesion force in the process were recorded. Adhesion energy could be obtained by integrating the stroke and adhesion curves (Fig. S38).

Drag simulation experiments

To obtain the actual swing of the pendant at the chest, we used a self-made motion measurement system to simulate and obtain the lateral and longitudinal displacements of the pendant (Fig. S14 and S39). The prepared flexible skin socket adhered to the skin-simulating silicon substrate, and the FPCB plug was attached to the socket to form the soft-stiff connection. Then the AGS-X system clamped the other end of the FPCB plug for lateral and longitudinal displacement to simulate the drag of the pendant (Fig. 3d). During this process, the drag loop was recorded and the attachment state was observed.

Dynamic 12-lead ECG acquisition test

For the MU-DCG system (250 Hz sampling rate), three healthy subjects were asked to wear the device and tested (all were male, aged 23, 24, and 26). A metronome was used to prompt the subject to perform a dynamic test at a specified speed. The "walk" status represents a dynamic walk of 90 steps/min, while the "jog" state requires subjects to move at a speed of 120 steps/min. In the "stair" test, subjects were asked to climb a 30-step staircase and return to the origin within 30 s. As for the "sit-still" status, subjects sat in a chair without any other movement. During these tests, the MU-DCG system transmitted real-time ECG data via Bluetooth to a laptop for recording by a self-developed host software built on Python 3.7 (or to a mobile phone for display with a digital high-pass filter, which is achieved through an app developed using Android Studio 4.0; Movie S2, Supplementary Methods). Besides, a 24-hour wearing test (one healthy subject, male, age 24) was carried out to prove the long-term comfortable wearing

experience and stable signal acquirement of the MU-DCG system (Figs. S40 and S41). For the Holter device test, a 12-lead LEPU MEDICAL dynamic 12-lead ECG recorder (256 Hz sampling rate) was used to carry out the test just the same as above. It meets the medical device standards (II class 07) of the National Medical Products Administration of China. During the testing process, the data of the system was stored on an SD card, and the data was read to analyze on a PC after each test. Furthermore, to investigate the impact of motion artifacts on ECG signal quality, we conducted simulations of skin compression and stretching, common sources of artifact during physical activity, using the all-in-one on-skin component of the MU-DCG system. These simulations, validated by testing on five subjects, showed that while the specific effects varied between individuals, the resulting artifacts were limited to minor baseline drift in the ECG signals, indicating robustness against common motion interference (Fig. S42).

Expert blind evaluation of the quality of ECG collected by the MU-DCG system

Expert evaluation includes two experiments based on blind methods. In the first experiment, 64 2 s ECG waveforms were randomly selected from a subject's 12-lead ECG data in the above dynamic ECG acquisition test, half of which came from the Holter device and the other half from the MU-DCG system (Fig. S24). After reordering, re-naming, and redrawing in the same format, five cardiologists scored them according to a criteria form (Table S4) and the statistical result is presented in Fig. 4F. For the second experiment, 192 beats (0.64 s) were randomly selected from a subject's 12-lead ECG data in the above dynamic ECG acquisition test, half from the Holter device and half from the MU-DCG system (Fig. S25). Similarly, after reordering, renaming, and redrawing in the same format, five cardiologists scored them according to the same criteria. The statistical result of the quality score for the heartbeats is shown in Fig. S43. Full details of the statistical analysis are provided in the Supplementary Methods.

The SNR (signal-noise ratio) computing and statistical methods

The 12-lead ECG data (data_initial) was first obtained by using a window sliding average (window length: $0.15 \times$ sampling rate, effectively acting as a low-pass filter, Fig. S44) to get the pre-processed raw data (data_a) to eliminate baseline drift. Subtracting the data_a from the data_initial gives the preprocessed raw data (data_b) with the offset removed. Then 0–50 Hz signals were extracted by "fft" and "ifft" functions in Matlab as imaginary pure signals (data_eff). Subtracted data_eff from data_b to get the noise data (data_noise). Finally, the "snr" function in Matlab R2023a was used to calculate the SNR (Fig. S45). Detailed statistical methods are provided in the Supplementary Methods.

Ethics

Every experiment involving human participants had been carried out following a protocol approved by an ethical commission. Each participant gave informed written consent.

Reporting summary

Further information on research design is available in the Nature Portfolio Reporting Summary linked to this article.

Data availability

The experimental data generated in this study are available and presented in the paper and the Supplementary Information. Any additional requests for information can be directed to, and will be fulfilled by, the corresponding authors. Source Data are provided with this paper. The collected ECG dataset acquired by this study is deposited in the supplementary data file S1–S2 and Zenondo database at https://doi.org/10.5281/zenodo.14586642 [51] Source data are provided with this paper.

Code availability

The code used to implement the classification tasks in this study is available from Zenodo (https://doi.org/10.5281/zenodo.14586642)[51].

References

1. GBD 2015 Mortality and Causes of Death Collaborators. Global, regional, and national life expectancy, all-cause mortality, and cause-specific mortality for 249 causes of death, 1980–2015: a systematic analysis for the global burden of disease study 2015. *Lancet.* **388**, 1459–1544 (2016).
2. Marijon, E. et al. The Lancet Commission to reduce the global burden of sudden cardiac death: a call for multidisciplinary action. *Lancet* **402**, 883–936 (2023).
3. Spatz, E. S. et al. Wearable digital health technologies for monitoring in cardiovascular medicine. *N. Engl. J. Med.* **390**, 346–356 (2024).
4. Tsao, C. W. et al. Heart disease and stroke statistics—2023 update: a report from the American Heart Association. *Circulation* **147**, e93–e621 (2023).
5. Virani, S. S. et al. 2023 AHA/ACC/ACCP/ASPC/NLA/PCNA guideline for the management of patients with chronic coronary disease: a report of the American Heart Association/American College of Cardiology Joint Committee on clinical practice guidelines. *Circulation* **148**, e9–e119 (2023).
6. Kennedy, H. L. The evolution of ambulatory ECG monitoring. *Prog. Cardiovasc. Dis.* **56**, 127–132 (2013).
7. Baig, M. M. et al. A comprehensive survey of wearable and wireless ECG monitoring systems for older adults. *Med. Biol. Eng. Comput.* **51**, 485–495 (2013).
8. Pal, S. et al. in *Encyclopedia of Biomedical Engineering*, R. Narayan, Ed. 363–379, (Elsevier, Oxford, 2019),
9. Yin, J. et al. Motion artefact management for soft bioelectronics. *Nat. Rev. Bioeng.* **2**, 541–558(2024).
10. Park, B. et al. Cuticular pad–inspired selective frequency damper for nearly dynamic noise–free bioelectronics. *Science* **376**, 624–629 (2022).
11. Hassan, M. F., Lai, D. & Bu, Y. in *Proceedings of the 2019 3rd International Conference on Computational Biology and Bioinformatics.* 76–79 (Association for Computing Machinery, 2019).
12. Barrett, P. M. et al. Comparison of 24-hour holter monitoring with 14-day novel adhesive patch electrocardiographic monitoring. *Am. J. Med.* **127**, 95.e11–95.e17 (2014).
13. Derkac, W. M. et al. Diagnostic yield of asymptomatic arrhythmias detected by mobile cardiac outpatient telemetry and autotrigger looping event cardiacmonitors. *J. Cardiovasc. Electrophysiol.* **28**, 1475–1478 (2017).
14. Zungsontiporn, N. & Link, M. S. Newer technologies for detection of atrial fibrillation. *BMJ-Brit. Med. J.* **363**, k3946 (2018).
15. Thygesen, K. et al. Fourth universal definition of myocardial infarction (2018). *Circulation* **138**, e618–e651 (2018).
16. Gibson, C. M. et al. Evolution of single-lead ECG for STEMI detection using a deep learning approach. *Int. J. Cardiol.* **346**, 47–52 (2022).
17. Zhang, J. et al. Activatable conformal electrode arrays for highly stable and breathable 12-lead clinical electrocardiographic monitoring. *Adv. Mater. Technol.* **8**, 2300243 (2023).
18. Lai, J. et al. Practical intelligent diagnostic algorithm for wearable 12-lead ECG via self-supervised learning on large-scale dataset. *Nat. Commun.* **14**, 3741 (2023).
19. Liu, C. et al. Signal quality assessment and lightweight QRS detection for wearable ECG smartvest system. *IEEE Internet Things J.* **6**, 1363–1374 (2019).
20. Li, Y. et al. Skin-adherent elastomer-hydrogel patch for continuous 12-lead cardiac ambulatory monitoring during physical activities. *Adv. Mater. Technol.* **8**, 2300326 (2023).

21. Sengupta, P. P. et al. The future of valvular heart disease assessment and therapy. *Lancet* **403**, 1590–1602 (2024).
22. Sempionatto, J. R. et al. An epidermal patch for the simultaneous monitoring of haemodynamic and metabolic biomarkers. *Nat. Biomed. Eng.* **5**, 737–748 (2021).
23. Zhu, Y. et al. A breathable, passive-cooling, non-inflammatory, and biodegradable aerogel electronic skin for wearable physical-electrophysiological-chemical analysis. *Adv. Mater.* **35**, 2209300 (2022).
24. Moin, A. et al. A wearable biosensing system with in-sensor adaptive machine learning for hand gesture recognition. *Nat. Electron.* **4**, 54–63 (2021).
25. Chung, U. U. et al. Binodal, wireless epidermal electronic systems with in-sensor analytics for neonatal intensive care. *Science* **363**, eaau0780 (2019).
26. Lee, S. et al. Nanomesh pressure sensor for monitoring finger manipulation without sensory interference. *Science* **370**, 966 (2020).
27. Su, Q. et al. A stretchable and strain-unperturbed pressure sensor for motion interference-free tactile monitoring on skins. *Sci. Adv.* **7**, eabi4563 (2021).
28. Jung, D. et al. Highly conductive and elastic nanomembrane for skin electronics. *Science* **373**, 1022–1026 (2021).
29. Yan, Z. et al. Highly stretchable van der Waals thin films for adaptable and breathable electronic membranes. *Science* **375**, 852–859 (2022).
30. Wang, Y. et al. Robust, self-adhesive, reinforced polymeric nano-films enabling gas-permeable dry electrodes for long-term application. *Proc. Natl Acad. Sci. Usa.* **118**, e2111904118 (2021).
31. Kim, D.-H. et al. Epidermal electronics. *Science* **333**, 838–843 (2011).
32. Liu, Y. et al. Epidermal mechano-acoustic sensing electronics for cardiovascular diagnostics and human-machine interfaces. *Sci. Adv.* **2**, e1601185 (2016).
33. Ma, X. et al. A monolithically integrated in-textile wristband for wireless epidermal biosensing. *Sci. Adv.* **9**, eadj2763 (2023).
34. Xu, H. et al. A fully integrated, standalone stretchable device platform with in-sensor adaptive machine learning for rehabilitation. *Nat. Commun.* **14**, 7769 (2023).
35. Kim, K. K. et al. A substrate-less nanomesh receptor with meta-learning for rapid hand task recognition. *Nat. Electron.* **6**, 64–75 (2023).
36. Miyamoto, A. et al. Inflammation-free, gas-permeable, lightweight, stretchable on-skin electronics with nanomeshes. *Nat. Nanotechnol.* **12**, 907–913 (2017).
37. Wang, Y. et al. Electrically compensated, tattoo-like electrodes for epidermal electrophysiology at scale. *Sci. Adv.* **6**, eabd0996 (2020).
38. Tian, L. et al. Large-area MRI-compatible epidermal electronic interfaces for prosthetic control and cognitive monitoring. *Nat. Biomed. Eng.* **3**, 194–205 (2019).
39. Jiang, Y. et al. A universal interface for plug-and-play assembly of stretchable devices. *Nature* **614**, 456–462 (2023).
40. Ma, Z. et al. Permeable superelastic liquid-metal fibre mat enables biocompatible and monolithic stretchable electronics. *Nat. Mater.* **20**, 859–868 (2021).
41. Lee, S. et al. Ultrasoft electronics to monitor dynamically pulsing cardiomyocytes. *Nat. Nanotechnol.* **14**, 156–160 (2019).
42. Li, D. et al. Lantern-inspired on-skin helical interconnects for epidermal electronic sensors. *Adv. Funct. Mater.* **33**, 2213335 (2023).
43. Kligfield, P. et al. Recommendations for the standardization and interpretation of the electrocardiogram: part I: the electro-cardiogram and its technology a scientific statement from the American Heart Association Electrocardiography and Arrhythmias Committee, Council on Clinical Cardiology; the American College of Cardiology Foundation; and the Heart Rhythm Society endorsed by the international society for computerized electrocardiology. *J. Am. Coll. Cardiol.* **49**, 1109–1127 (2007).
44. Luna, A. B. d. et al. *Clinical Electrocardiograph. Martinus Nijhoff Publishers*: Dordrecht, The Netherlands, (2012).
45. Rautaharju, P. M. et al. AHA/ACCF/HRS recommendations for the standardization and interpretation of the electrocardiogram: Part IV: The ST segment, T and U waves, and the QT interval: A scientific statement from the American heart association electrocardiography and arrhythmias committee, council on clinical cardiology; the American college of cardiology foundation; and the heart rhythm society: endorsed by the international society for computerized electrocardiology. *Circulation* **119**, e241–e250 (2009).
46. Liu, J. et al. BioAIP: a reconfigurable biomedical AI processor with adaptive learning for versatile intelligent health monitoring. *2021 IEEE Int. Solid-State Circ. Conf.* 62–64 (2021).
47. Liu, J. et al. An ultra-low power reconfigurable biomedical AI processor with adaptive learning for versatile wearable intelligent health monitoring. *IEEE Trans. Biomed. Circuits Syst.* **17**, 952–967 (2023).
48. Zhuang, Q. et al. Permeable, three-dimensional integrated electronic skins with stretchable hybrid liquid metal solders. *Nat. Electron.* **7**, 598–609 (2024).
49. Zhuang, Q. et al. Wafer-patterned, permeable, and stretchable liquid metal microelectrodes for implantable bioelectronics with chronic biocompatibility. *Sci. Adv.* **9**, eadg8602 (2023).
50. Song, Y. et al. 3D-printed epifluidic electronic skin for machine learning–powered multimodal health surveillance. *Sci. Adv.* **9**, eadi6492 (2023).
51. Ding, L. et al. Source data and codes of "Motion-unrestricted dynamic electrocardiogram system utilizing imperceptible electronics"(v.3) (Zenodo, https://doi.org/10.5281/zenodo.14586642 (2024).

Acknowledgements

Author contributions

T.-L.R., J.Z., Y.Y., H.-F.L., and D.L. determined the conceptualization direction. D.L., T.-R.C., J.-H.L., and W.-C.S planned the experimental method. D.L., T.-R.C., J.-H.L., W.-C.S., X.L., Z.-K.C., X.L., L.-Q.T., and Z.-W.C. discussed and finished the investigation before the experiment. D.L., T.-R.C., J.H.L., W.-C.S., X.L., Z.-K.C., Z.-G.X., X.L., S.-Y.X., J.-M.J., Z.-Y.X., X.W. participated in the visualization works. T.-L.R, J.Z., Y.Y., H.-F.L., X.-M.W., and X. L were responsible for funding acquisition. T.-L.R., J.Z., Y.Y., and H.-F.L. conducted project administration and supervision. D.L., T.-R.C., J.-H.L., W.-C.S., X.L., and Z.-K.C. wrote the original draft. D.L., H.-F.L., T.-R.C., J.-H.L., Z.-G.X., X.L., S.-Y.X., J.-M.J., Z.-Y.X., L.-Q.T., X.-M.W., and Z.-R.D. reviewed and edited the original manuscript. All authors read and revised the manuscript.

Competing interests

Additional information